Water Air Soil Pollut (2023) 234:18
https://doi.org/10.1007/s11270-022-05978-y

Efficiency of TiO_2/Fe_2NiO_4 Nanocomposite in Photocatalytic Degradation of Acid Orange 7 (AO7) Under UV Irradiation

Inshad Jum'h · Rashed Abu-Aleqa · Rami Jumah · Carlos J. Tavares · Ahmad Telfah

Received: 4 May 2022 / Accepted: 18 November 2022 / Published online: 27 December 2022

Abstract A novel coupling of titanium dioxide (TiO_2) with iron-nickel oxide (Fe_2NiO_4) nanoparticles (NPs) is attained in this work by solid state blending technique and investigated as a promising photocatalyst for textile wastewater treatment. The NPs were examined to identify the crystalline structure, surface morphology, and size distribution. The photodegradation of highly concentrated acid orange 7 (AO7) aqueous solution under UV-irradiation was optimized for both NPs coupling ratio and solution acidity (pH). Coupling TiO_2 with Fe_2NiO_4 led to the enhancement by 87% of the first-order kinetic rate constant (k) of the photocatalytic reaction, when compared to that of only TiO_2 NPs. Under optimized conditions, complete color removal of 50 mg/L AO7 aqueous solution was successfully achieved after 40 min of UV- irradiation using only 100 mg/L of TiO_2/Fe_2NiO_4 with the optimized ratio of 2 wt.% of Fe_2NiO_4 with respect to TiO_2, where it was associated to the best photocatalytic degradation process of AO7 under UV-irradiation. Moreover, the AO7 solution with pH= of 9 shows the highest degradation performance, while the degradation at pH of 3 and 12 is comparable and significantly higher than the quasi neutral solution (pH equal to 6.5). For optimized conditions, the electrical energy consumption at the optimized conditions, expressed as electric energy per order, is 50.3 kWh/m^3.

Keywords Titanium dioxide (TiO_2) nanoparticles · Iron-nickel oxide (Fe_2NiO_4) nanoparticles · Acid orange 7 (AO7) · Photocatalytic degradation · Industrial wastewater

I. Jum'h
School of Basic Science and Humanities, German-Jordanian University (GJU), Amman 11180, Jordan

R. Abu-Aleqa · R. Jumah
Department of Chemical Engineering, Jordan University of Science and Technology, Irbid 22110, Jordan

C. J. Tavares
Centre of Physics of Minho and Porto Universities, University of Minho, 4804-533 Guimaraes, Portugal

A. Telfah (✉)
Leibniz-Institut für Analytische Wissenschaften – ISAS – e.V., 44139 Dortmund, Germany
e-mail: telfah.ahmad@isas.de

A. Telfah
Nanotechnology Center, The University of Jordan, Amman 11942, Jordan

1 Introduction

Dyes pose a significant risk owing to their non-biodegradability, toxicity, and carcinogenicity (Suzuki et al., 2020) and impacting humans by affecting the ecosystem and ground water resources (Al-Tohamy et al., 2022; Manzoor & Sharma, 2020). Essentially, dyes are intentionally designed to resist biodegradation to prevent the vanishing of colors over time (Zaheer et al., 2019). Synthetic dyes are extensively

used in many industries such as textile, dyeing, pharmaceutical, paper printing, color photography, food, cosmetics, and other process industries (Samsami et al., 2020; Silva et al., 2021). It is reported that over 7×10^5 tons of dyes and pigments, including more than 100,000 commercially available dyes, are produced worldwide every year (Perera, 2019). Due to the toxicity, biodegradability, and persistent nature of these dyes, their elimination from wastewater has become an important issue in recent years (Rashid et al., 2021; Santhosh et al., 2016). There are only a few effective technologies capable of cleaning dye-containing wastewater, through adsorption and biological methods, as well as advanced oxidation processes (AOPs) (Hossen et al., 2022; Thekkedath et al., 2022). In contrast to adsorption and biological methods, AOPs are efficient, low-cost, and applicable to small and large-scale industries. Among the AOPs, the heterogeneous photocatalytic process employing TiO_2 nanoparticles (NPs) as photocatalsysts is a promising technology that has shown efficient dye removal from wastewater (Al-Mamun et al., 2019; Iervolino et al., 2020). Unfortunately, the practical application of unmodified TiO_2 nanoparticles is limited; because of the wide bandgap (3.0–3.2 eV), it is mostly active under the ultra-violet irradiation (wavelength < 410 nm), which is less than 5% of the total solar spectrum and, thus, it lacks the ability to take advantage of using the visible light provided by the sun. Moreover, the photocatalytic efficiency is reduced by the rapid electron–hole pair recombination due to the low quantum efficiency of TiO_2 (Khasawneh & Palaniandy, 2021; Rehman et al., 2009). To overcome these limitations, doping TiO_2 with metals and coupling it with other semiconductors have been developed, which effectively improve the photocatalytic activity of TiO_2 under UV, visible and direct sun irradiations (Haider et al., 2019; Nasr et al., 2018).

Nguyen et al. (Nguyen et al., 2018) used palladium-doped TiO_2 to enhance photocatalytic degradation of methylene blue (MB) and methyl orange (MO) under UV- irradiation, achieving 99.4% and 92.6% degradation of MB and MO using 0.5 wt.% and 0.75 wt.% Pd-TiO_2, respectively, after 2 h. McManamon et al. (McManamon et al., 2015) reported the synthesis of S-doped TiO_2 nanoparticles through a facile synthesis route, which effectively narrowed the bandgap of TiO_2 from 3.2 to 1.7 eV. It was observed that malachite green (MG) dye the optimum S-doped TiO_2 (20 mg/L degradation) surpassed undoped TiO_2 (16 mg/L degradation) and commercially available P25 (degradation), under the same conditions. Recently, Han et al. (Han et al., 2018) studied the photocatalytic degradation of acid orange 7 (AO7) using Fe^{+3} doped TiO_2 nanoparticles under different irradiation sources, UV, visible and solar lights. The prepared doped catalyst showed a slight improvement under UV-irradiation compared with undoped TiO_2, while a huge improvement was observed under visible and solar irradiations. By using UV-irradiation, they achieved complete degradation of 50 mg/L AO7 after 2 h using 100 mg/L of 3 wt.% Fe^{+3} doped TiO_2. Using visible light, 25 mg/L AO7 was completely degraded after 6 h of visible light irradiation using 500 mg/L of 2 wt.% Fe^{+3} doped TiO_2, while only 5 mg/L AO7 was degraded using undoped TiO_2 under the same conditions.

In this study, the enhancement of the photocatalytic degradation was investigated by coupling TiO_2 NPs with iron-nickel oxide (Fe_2NiO_4) nanoparticles under UV-irradiation. The process conditions were optimized for the coupling ratio and pH of the solution. Since azo dyes account for more than half of all dyes produced annually and in common use (Chung, 2016), Acid Orange 7 was selected as test pollutant for the degradation process as an effective model representing industrial wastewater containing azo dyes.

2 Experiment

2.1 Chemicals

Acid Orange 7 (AO7) ($C_{16}H_{11}N_2NaO_4S$) (Fig. 1), TiO_2 nanoparticles (anatase-phase crystal structure with an average particle size of about 25 nm), and iron-nickel oxide nanoparticles (Fe_2NiO_4 NPs with an average particle size of about 50 nm) were purchased from Sigma-Aldrich. Chemical oxygen demand (COD) reagents: Potassium dichromate, Mercury (II) sulfate, sulfuric acid were purchased from Scharlau Chemicals. pH adjustment chemicals: Sodium hydroxide was purchased from Daejung reagents and chemicals, and hydrochloric acid 37% was purchased from Carlo Erba reagents. All chemicals were of analytical grade and were used without further purification.

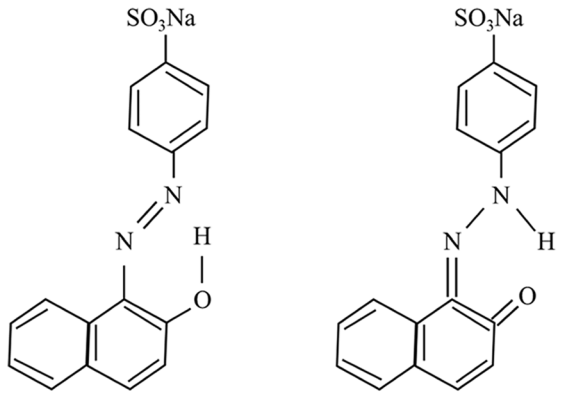

Fig. 1 The chemical structure of the AO7in (**a**) Azo and (**b**) Hydrazone forms

Table 1 Blending ratio of the prepared $100TiO_2$:xFe_2NiO_4 nanocomposite, where x is the absolute weight of Fe_2NiO_4 with respect to 100 folds of the absolute weight of TiO_2 to get the values in weight percentage (wt.%)

Composite	TiO_2 NPs [mg]	Fe_2NiO_4 NPs [mg]	Nanocomposite
1	100	0	pure TiO_2
2	100	1	$100TiO_2$:$1Fe_2NiO_4$
3	100	2	$100TiO_2$:$2Fe_2NiO_4$
4	100	3	$100TiO_2$:$3Fe_2NiO_4$
5	100	4	$100TiO_2$:$4Fe_2NiO_4$
6	100	8	$100TiO_2$:$8Fe_2NiO_4$
7	100	20	$100TiO_2$:$20Fe_2NiO_4$

2.2 Preparation of TiO_2/Fe_2NiO_4 Nanocomposite

TiO_2/Fe_2NiO_4 nanocomposite was prepared using the solid-state-blending in a particular ration (Table 1) using a pestle in an agate mortar for 30 min at room temperature (25 ℃). Afterward, the blended TiO_2/Fe_2NiO_4 nanocomposite was heated at 200 ℃ for 1 h, promoting the TiO_2/Fe_2NiO_4 nanocomplex coupling.

2.3 TiO_2/Fe_2NiO_4 Nanocomposite Characterization

An X-ray diffractometer (Ultima IV, Rigaku) was used to identify the crystalline structure of the samples using Cu Kα radiation. The size and the morphology of the TiO_2/Fe_2NiO_4 nanocomposite were evaluated using Quanta FEG 450 scanning electron microscopes (SEM). Zeta Sizer Nano-ZS90 (Malvern Panalytical) was used to determine the size distribution of the photocatalytic nanocomposite dispersed in water.

2.4 Photocatalytic Degradation Experiments and Characterizations

A customized photocatalytic reactor (model TL-GHX-II, China) (Fig. 2a and b) was employed for photocatalytic removal of AO7 in an aqueous solution. It was designed in such a way that the radiation source is immersed within the solution, allowing for maximum energy transfer from the source to the solution. The reactor has a maximum volume of 2 L and is connected to a chiller for lamp cooling. The power of the UV lamps is up to 1000 W. The UV–irradiation is emitted using a mercury lamp that produces light with maximum intensity at a wavelength of 365 nm.

The photocatalytic degradation of 50 mg/L AO7 aqueous solutions in 1.8 L of water using TiO_2, Fe_2NiO_4, and TiO_2:xFe_2NiO_4 nanocomposites was investigated. In this study, an optimum catalyst loading of 100 mg/L was used based on the literature recommendation (Santhosh et al., 2016). Reaction conditions were optimized in terms of TiO_2/Fe_2NiO_4 NPs coupling ratio and pH. Polyacrylic acid (PAA) polymer was used in 300 mg/1.8 L water as a coating agent for nanoparticles to improve their suspension stability and prevent the particle agglomeration. Then, the desired quantity of catalyst was added to the solution and stirred for 15 min. After that, the solution was sonicated using a bath (Elmasonic P) for 10 min at low frequency (37 Hz) and power of 500 Watt. Afterwards, the solution was stirred for another 30 min, and immediately, 50 mg/L AO7 was added. The solution acidity was adjusted to pH = 3 and was stirred in the dark for 45 min, allowing adsorption of AO7 onto the catalyst surface to take place.

For UV–Vis absorbance measurements, samples were taken at time intervals (5–30 min), filtered using a syringe filter (Filter-Bio PTFE-L), and direct UV–Vis absorbance spectra were acquired through a spectrophotometer (Beckman DU520). Simultaneously, from the sample batch allocated for UV–Vis experiments, the chemical oxygen demand (COD) was determined using the standard dichromate method. Prepared digestion solution (dichromate) and sulfuric acid reagents were added in the

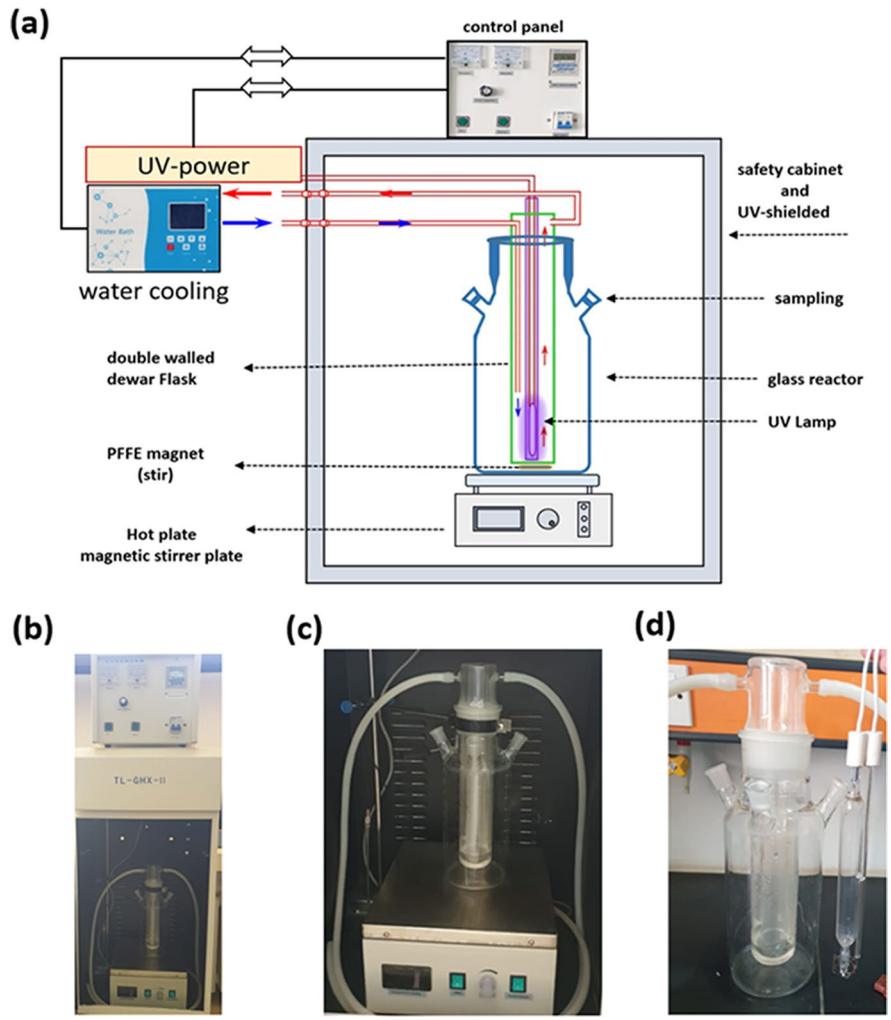

Fig. 2 (**a**) A schematic of the photocatalytic-glass-reactor including the safety cabinet-UV-shielding, control panel, UV-power, hot plate including the magnetic stirrer plate and PTFE coated magnets, double walled-dewar-glass and water cooling system. (**b**) The setup of the customized photocatalytic reactor assembly, (**c**) the enlargement of the reactor and (**d**) the glass-photocatalytic reactor with UV-lamp disassembled

proper amounts to the samples, including a blank. Subsequently, the solution was incubated at 150 °C for 120 min in a COD digester (thermo-reactor RD 125, Lovibond), being the COD measurements performed using a spectrophotometer (MultiDirect, Lovibond). The pH was measured using a Mettler Toledo SevenGo Duo pH/Cond meter SG23 pH meter.

The electrical energy consumption of the photocatalytic reactions was determined by electric energy per order (E_{EO}), which represents the energy in kilowatt-hours (kWh) required to remove contaminant X by one order of magnitude (90%) in 1 m^3 of contaminated water. The E_{EO} value was calculated using the following equation (Bolton et al., 2001):

$$E_{EO} = \frac{P \cdot t \cdot 1000}{V \cdot 60 \cdot ln(\frac{C_o}{C_f})}$$

where E_{EO} is the electric energy per order (kWh/m^3); P is the nominal power of the light source (kW) (500 W mercury lamp); t is the irradiation time (minutes) (25 min to achieve 90% removal); C_0 and C_f are the AO7 initial and final concentrations (mg/L), and V is the solution volume (1.8 L).

X-ray diffraction analysis (XRD, Malvern Panalytical Ltd, Malvern, UK) and scanning electron microscopy (SEM, FEI Quanta FEG 450) were used to investigate the structural and morphological properties of pure TiO_2 NPs, pure Fe_2NiO_4 NPs, and $100TiO_2$:xFe_2NiO_4 NPs (x = 2 wt.%) and x = 3 wt.%) deposited on silicon substrate. Moreover, SEM–EDX (Phenom Pro/ProX G6; nanoScience instruments) were used to acquire micrographs and average energy dispersive spectroscopy (EDX) measurements for pure TiO_2 NPs, pure Fe_2NiO_4 NPs, and $100TiO_2$:xFe_2NiO_4 NPs (x = 2 wt.% and x = 3 wt.%) deposited on conductive carbon adhesive tape. Optical properties including transmittance and reflectance spectra and other corresponding parameters were investigated using a double-beam UV–Vis spectrophotometer (Hitachi U-3900H) with a total internal sphere.

3 Results and Discussion

3.1 X-ray Diffraction

X-ray diffraction (XRD) patterns of pure TiO_2 NPs, pure Fe_2NiO_4 NPs, and TiO_2/Fe_2NiO_4 nanocomposite samples at 2θ = 20°–90° are shown in Fig. 3. XRD pattern of pure TiO_2 and its composites exhibit main peaks at 2θ = 25.00, 37.56°, 47.76°, 53.63°, 54.86°, and 62.32° corresponding to the planes (101), (004), (200), (105), (211), (213), respectively (Ijadpanah-Saravy et al., 2014), which matches with the anatase phase TiO_2. It should be noted that the Bragg positions and relative intensities of the diffraction peaks are consistent with the standard pattern for JCPDS Card No. (21–1272) and with reported literature on TiO_2 (Robotti et al., 2016). The TiO_2 rutile phase was not observed; this confirms the well-crystallized single anatase phase of TiO_2 used throughout this

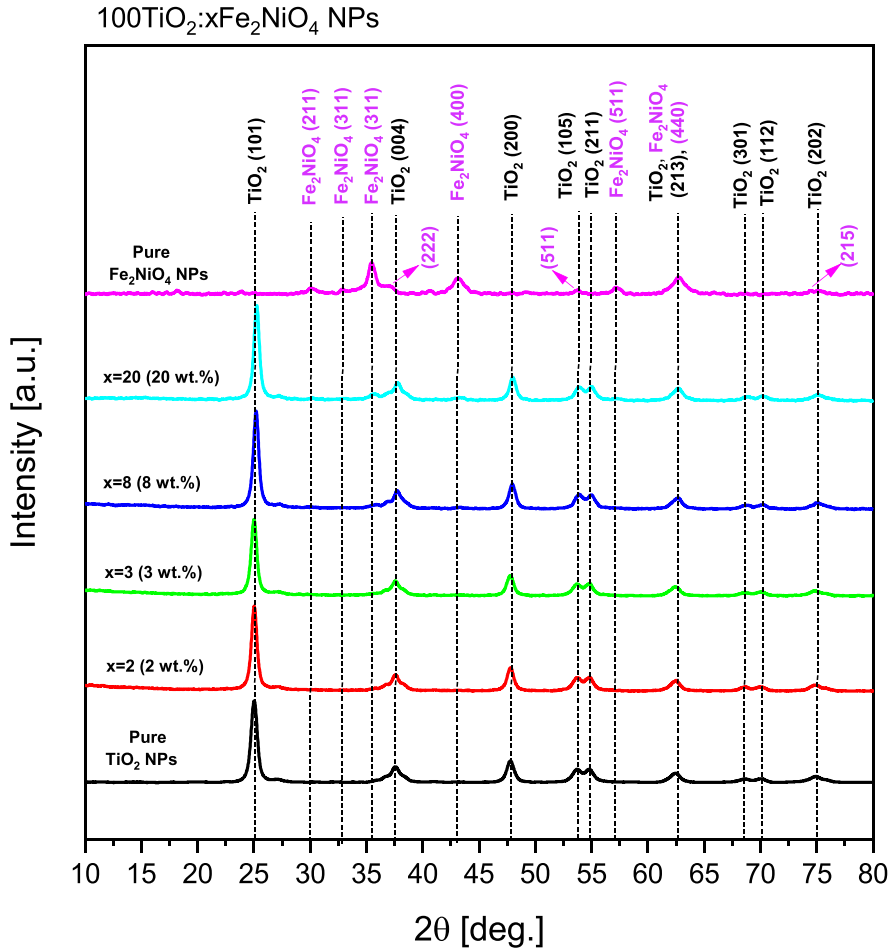

Fig. 3 XRD patterns of TiO_2/Fe_2NiO_4 NPs with different coupling ratios of Fe_2NiO_4 NPs

study. As noticed from Fig. 3, combining Fe_2NiO_4 NPs in small fractions with TiO_2 NPs resulted in additional lower-intensity diffraction peaks, indicative of the low Fe_2NiO_4 content in the coupled samples. In addition, the intensities of the major peaks of TiO_2 NPs decreased with increasing the coupling ratio of Fe_2NiO_4 NPs, while, in the coupled samples, an increase in intensities was observed. Finally, new peaks at $2\theta = 37.3°$ corresponding to Fe_2NiO_4 (311) were observed, indicating the presence of iron in the coupled TiO_2 NPs with higher amounts of Fe_2NiO_4 NPs (Habibi & Fakhri, 2017).

Crystal parameters such as crystallite size (D), microstrain $\langle\varepsilon\rangle$, the density of dislocations (δ), total internal stress (σ), and strain energy density (E_d) were calculated from the XRD data according to the formulas listed in Table 2 (Al-Bataineh et al., 2019, 2020a; Alsaad et al., 2020). The crystallite size of the pure TiO_2 NPs is 12 nm. The largest (14 nm) and smallest (11 nm) crystallite size are registered for x = 2 wt.% and x = 3 wt.%, respectively. The microstrain shows opposite trend of the crystallite size and the inverse dependence of the microstrain on the crystallite size is related to the reduction in the volume occupied by the atoms inside the joint crystalline structure. As a result, the latter observation leads to an increase in the unit cell volume, which causes in-plane positions shifts and dislocations (Horiuchi et al., 2010), playing a significant role in the materials strength and ductility (Akl & Hassanien, 2015). δ characterizes the crystalline clusters-spaces and their agglomerations since a reduction in δ indicates an enhancement in the crystallization and lessening of the free spaces (Akl & Hassanien, 2015; Williamson & Smallman, 1956). δ of pure TiO_2 NPs is 7.15×10^{11} lines/cm^2 and, likewise the microstrain, the highest δ of TiO_2/Fe_2NiO_4 NPs was at 3 wt.%, and the lowest δ was at 2 wt.%. The values of the total internal stress and strain energy density of pure TiO_2 NPs are 4.99×10^8 N/m^2 and 8.25×10^5 J/m^3, respectively.

3.2 SEM Analysis

Scaning electron microscopy (SEM) micrographs of pure TiO_2 NPs, pure Fe_2NiO_4 NPs, and $100TiO_2$:xFe_2NiO_4 NPs (x = 2 wt.%) and x = 3 wt.%) deposited on silicon substrate are demonstrated in Fig. 4a–d. The size distributions were calculated statistically by measuring the diameters randomly in the micrograph. TiO_2 NPs in $100TiO_2$:$2Fe_2NiO_4$ and $100TiO_2$:$3Fe_2NiO_4$ nanocomposites are spherical, with size distributions between 15 and 25 nm while for pure Fe_2NiO_4, are also spherical with sizes in the range of 30–50 nm.

Additionally, in Fig. 5, SEM micrographs and average energy dispersive spectroscopy (EDX) measurements were acquired for pure TiO_2 NPs, pure Fe_2NiO_4 NPs, and $100TiO_2$:xFe_2NiO_4 NPs (x = 2 wt.% and x = 3 wt.%) deposited on conductive carbon adhesive tape.

EDX measurements and respective analysis were performed on the entire area displayed in the SEM micrographs. The EDX results are in agreement with the preparation approach (2 and 3 wt.%). The elemental carbon in the EDX analysis is from the conductive carbon adhesive tapes substrate and the carbon percent is high according to the powder coverage of the substrate, while the elemental sulfur and magnesium are impurities in the nanoparticles.

Table 2 Crystallographic parameters of TiO_2/Fe_2NiO_4 NPs with different coupling ratios of Fe_2NiO_4 NPs

Parameters	Formula	Fe_2NiO_4 (0 wt.%)	Fe_2NiO_4 (2 wt.%)	Fe_2NiO_4 (3 wt.%)	Fe_2NiO_4 (8 wt.%)	Fe_2NiO_4 (20 wt.%)
Crystallite size (D) [nm]	$D = k\lambda/\beta cos\theta$ 12	14	11	12	12	
Micro-strain ($\langle\varepsilon\rangle \times 10^{-3}$)	$\langle\varepsilon\rangle = \beta cot\theta/4$ 3.3	2.9	4.0	3.4	3.4	
Dislocation density ($\delta \times 10^{11}$) [lines/cm^2]	$\delta = 1/D^2$ 7	5	9	7	7	
Total internal stress ($\sigma \times 10^8$) [N/m^2]	$\sigma = E\langle\varepsilon\rangle$ 5.0	4.4	6.1	5.2	5.2	
Strain energy density ($E_d \times 10^5$) [J/m^3]	$E_d = \frac{1}{2}E\langle\varepsilon\rangle^2$ 8.3	6.4	12.5	8.8	8.9	

λ is the wavelength of the X-ray (λ = 0.154184nm), β is the full width at half maximum (FWHM) (β expressed in radians), θ is the Bragg angle, and k is Scherrer constant equal 0.9, E is Young's Modulus

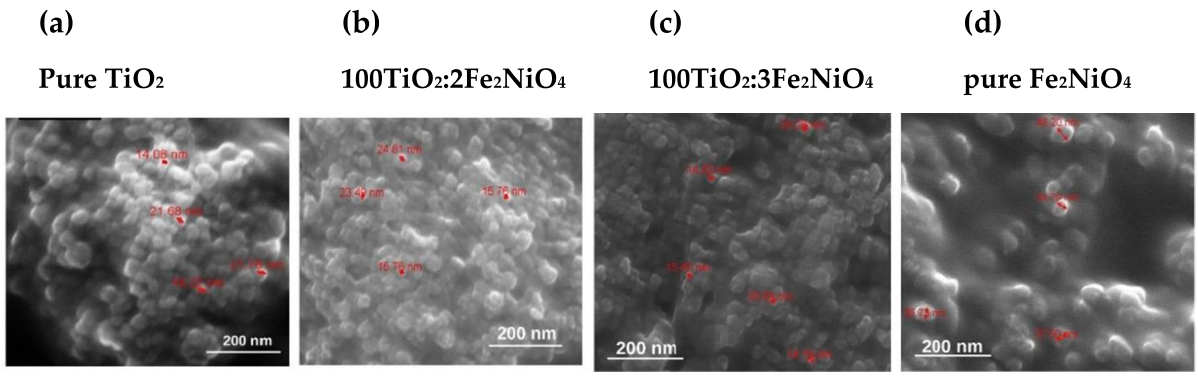

Fig. 4 SEM micrographs and size analysis of (**a**) pure TiO_2 NPs, (**b**) $100TiO_2{:}2Fe_2NiO_4$, (**c**) $100TiO_2{:}3Fe_2NiO_4$ and (**d**) pure Fe_2NiO_4 NPs

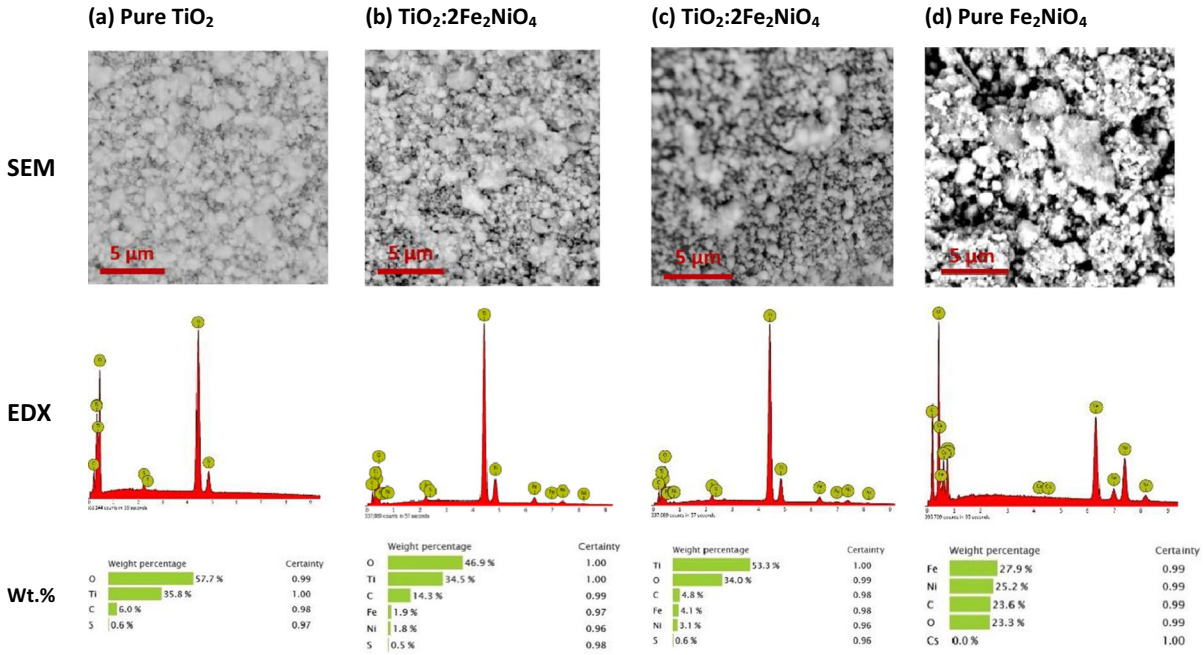

Fig. 5 SEM micrographs, EDAX, and elemental analysis of (**a**) pure TiO_2 NPs, (**b**) $100TiO_2{:}2Fe_2NiO_4$, (**c**) $100TiO_2{:}3Fe_2NiO_4$ and (**d**) pure Fe_2NiO_4 NPs

3.3 Dynamic Light Scattering

The nanoparticle aggregation distributions in aqueous solutions for pure TiO_2 NPs, $100TiO_2{:}2Fe_2NiO_4$, $100TiO_2{:}3Fe_2NiO_4$ nanocomposite NPs and pure Fe_2NiO_4 NPs was characterized based on the size (NPs diameter) using Dynamic Light Scattering (DSL) (Fig. 6) and compared to the size distribution deduced from SEM. The diameters deduced from DLS were 260 nm, 324 nm, 232 nm, and 262 nm, respectively, corresponding to pure TiO_2 NPS, $100TiO_2{:}2Fe_2NiO_4$ NPs, $100TiO_2{:}3Fe_2NiO_4$ NPs, and pure Fe_2NiO_4 NPs samples, which are larger than the particle size obtained from SEM for the same samples; this is because nanoparticles tend to aggregate in aqueous solution.

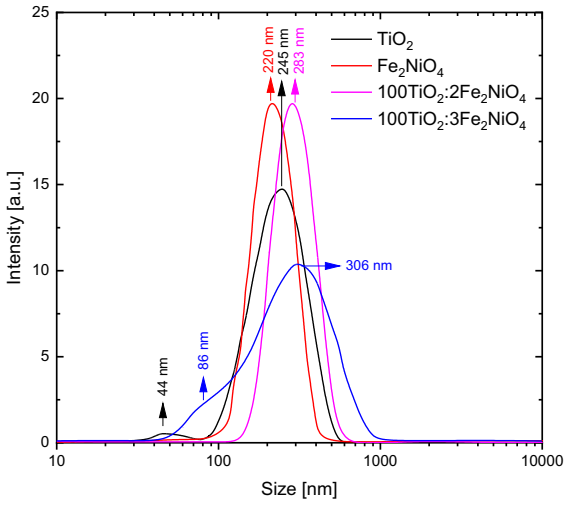

Fig. 6 Size distribution measurements of pure TiO_2 NPs, $100TiO_2$:$2Fe_2NiO_4$ NPs, $100TiO_2$:$3Fe_2NiO_4$ NPs and pure Fe_2NiO_4 NPs using DLS

3.4 Photocatalytic Activity Under UV-Irradiation

The UV–Vis spectra of the AO7 aqueous solution as a function of degradation time during the are shown in Fig. 7. UV–Vis absorption spectrum of AO7 exhibits 4 peaks at 230 nm, 256 nm, 308 nm, 482 nm, and a shoulder peak at 430 nm. The presence of hydrazone form is confirmed based on the characteristic peak at 482 nm, whereas the shoulder at 430 nm is associated with the transition of the azo form (Bauer et al., 1999). The two other peaks at 230 nm and 308 nm are attributed to the benzene and naphthalene rings of AO7 molecules (Feng et al., 2000). The absorbance at 482 nm was used to monitor the decolorization of AO7, while the peaks at 230 nm and 308 nm were used to indicate the decomposition of the aromatic moieties of AO7. Noticeably, after 120 min of illumination, the 4 characteristic peaks of AO7 vanished completely and no new peaks were formed, indicating the complete degradation of AO7.

In Fig. 8a , the normalized amplitude of absorbance spectra at 482 nm as a function of irradiation time (represented in scattered points) is fitting to the first-order kinetics model using the formula ($C/C_0 = exp(-kt)$) (represented in solid lines). As the result of the fitting, the first-order reaction rate constants (k) were deduced and plotted versus the Fe_2NiO_4 NPs wt.% in Fig. 8b ; The best enhancement is observed at coupling rate with Fe_2NiO_4 NPs of 2 wt.% with relative improvement of 87% compared to pure TiO_2 NPs. The most probable explanation could be based on the enhancement of electron–hole pairs separation at 2 wt.%, where, typically, Fe_2NiO_4 acts as an electron acceptor. Remarkably, at 4 wt.% has the lowest performance between the nanocomposite nanoparticles, but still higher than for pure TiO_2.

Under the same conditions (100 mg/L catalyst dose, 50 mg/L AO7, and pH = 3), Han et al. (Han et al., 2018) have achieved comparable results by doping TiO_2 NPs with Fe^{3+}. The highest rate constant ($k = 0.023$ min^{-1}) was observed for $100TiO_2$:$20Fe_2NiO_4$ photocatalyst; still, this value is lower than that obtained with coupling with low amounts of Fe_2NiO_4 (optimum $100TiO_2$:$2Fe_2NiO_4$, $k = 0.025$ min^{-1}).

The UV–Vis absorbance spectral evolution (Fig. 7) does not seem to indicate a consecutive attenuation process in the absorbance maxima according to irradiation time, since these maxima comprise more than a single absorption peak (frequency band). If the experimental absorption curve was a single peak, then the long exposure of irradiation should simply decrease the amplitude and increase the absorbance linewidth. Spectral analysis was performed to quantify the several frequency absorbance bands of the AO7 over the 25 min of UV–irradiation using TiO_2/Fe_2NiO_4 NPs with different concentrations of Fe_2NiO_4. The latter spectra were specifically selected over other degradation times because all the functional groups and moieties lines in the spectra of AO7 and intermediate smaller molecules were still present with proper intensity for fitting. The degradation process had already started, implying that all the intermediate species are present. The results show non-monotonic spectral dynamics, including peak wavelength shifts, absolute amplitude, and area changes for the AO7 bands, which suggests the cleavage of an azo bond is not the only or the dominant process.

Because of the frequency bands convolution, the spectral parameters are accordingly highly correlated, and the baseline is modulated. A rigorous regressions approach was applied to achieve fitting convergence. Figure 9a–h shows the significant peaks in the spectrum of the UV–Vis fitted to six Gaussian peaks; the fitting converged to the deconvoluted line describing adequately the experimental data. Baseline correction was done by a second derivative method using

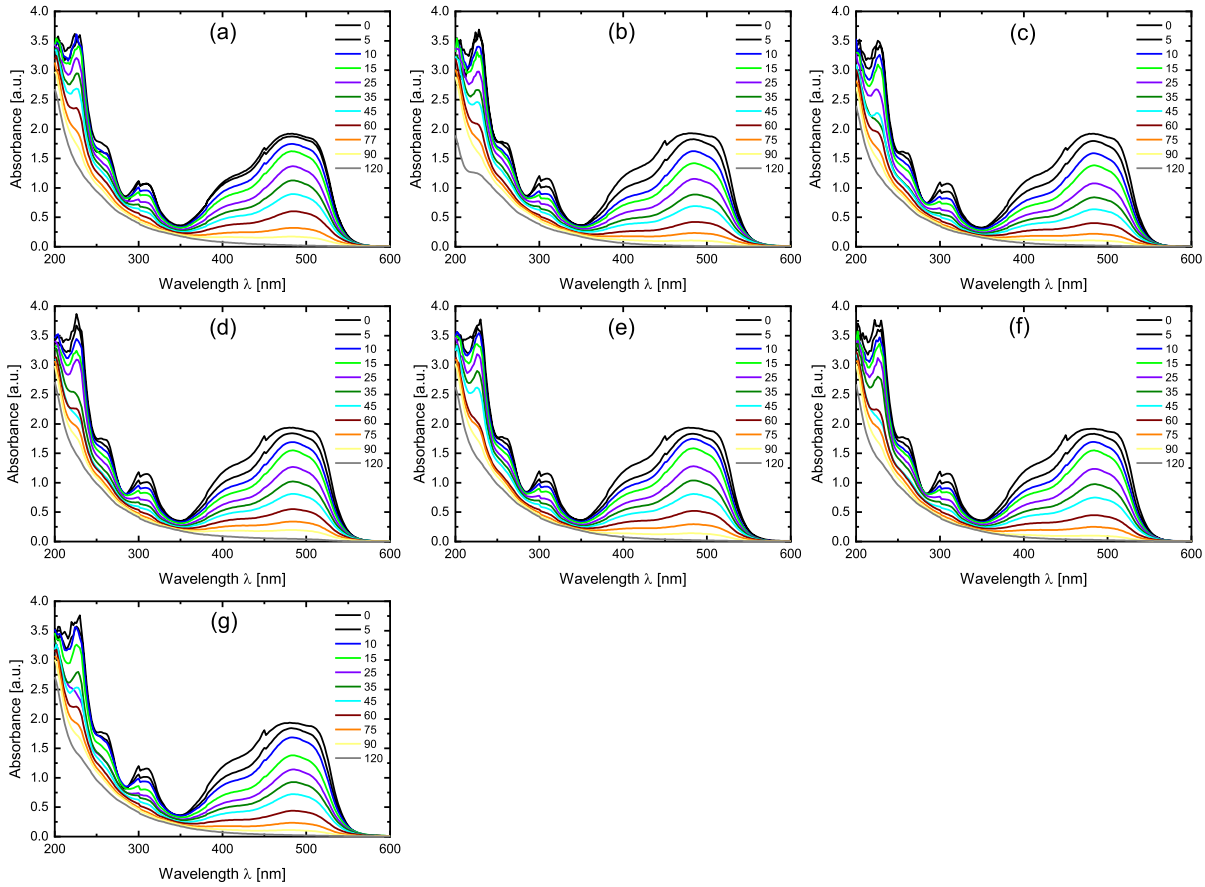

Fig. 7 UV–Vis absorbance spectra versus wavelength as a function of UV-irradiation time for (**a**) pure TiO_2 NPs, (**b**) $100TiO_2$:$1Fe_2NiO_4$, (**c**) $100TiO_2$:$2Fe_2NiO_4$, (**d**) $100TiO_2$:$3Fe_2NiO_4$ NPs, (**e**) $100TiO_2$:$4Fe_2NiO_4$ NPs, (**f**) $100TiO_2$:$8Fe_2NiO_4$ NPs, and (**g**) $100TiO_2$:$20Fe_2NiO_4$ NPs, pH = 3, AO7 concentration = 50 mg/L and 100 mg/L catalyst dose

OriginLab software, in which the fit was found to be inadequate compared with other baseline algorithms, such as polynomial or linear functions.

In the first state (Fig. 9a), the absorption band at 515 nm corresponding to the $n-\pi^*$ transitions of the hydrazone form, while the bands at 473 nm and 404 nm corresponding to the $n-\pi^*$ transitions of the azo form of the dye in the *trans*- and *cis*-states, respectively. These bands are due to the chromophore containing azo-linkage. It is clear that the *trans*-state in the azo form dominates compared with the *cis*-state, due to that the *trans*-state is more stable at room temperature (Ahmad et al., 2021a). The absorption bands at 308 nm and 262 nm are assigned to the $\pi-\pi^*$ transition in the naphthalene ring. The energy difference between the two peaks can be attributed to the naphthalene rings in the two cases; azo form and hydrazone form (Maeda et al., 2012), and finally, the absorption band at 229 nm is assigned to the $\pi-\pi^*$ transition in benzene ring (Ahmad et al., 2021b; Lau et al., 2014). The shape of the absorption spectrum changed after 25 min of UV–irradiation for all NPs combinations as deduced by the progressing divergence of the all-bands linewidth of the Gaussian function (Fig. 9). Pure TiO_2 and TiO_2/Fe_2NiO_4 NPs with different concentrations of Fe_2NiO_4 were affected similarly on all frequency bands with different variations in the area of the bands. TiO_2/Fe_2NiO_4 NPs of 2 wt.% Fe_2NiO_4 was the most effective sample (Fig. 10). So, the time evolution of the AO7 spectrum using TiO_2:$2Fe_2NiO_4$ NPs (2 wt.% of Fe_2NiO_4) as a catalyst were analyzed.

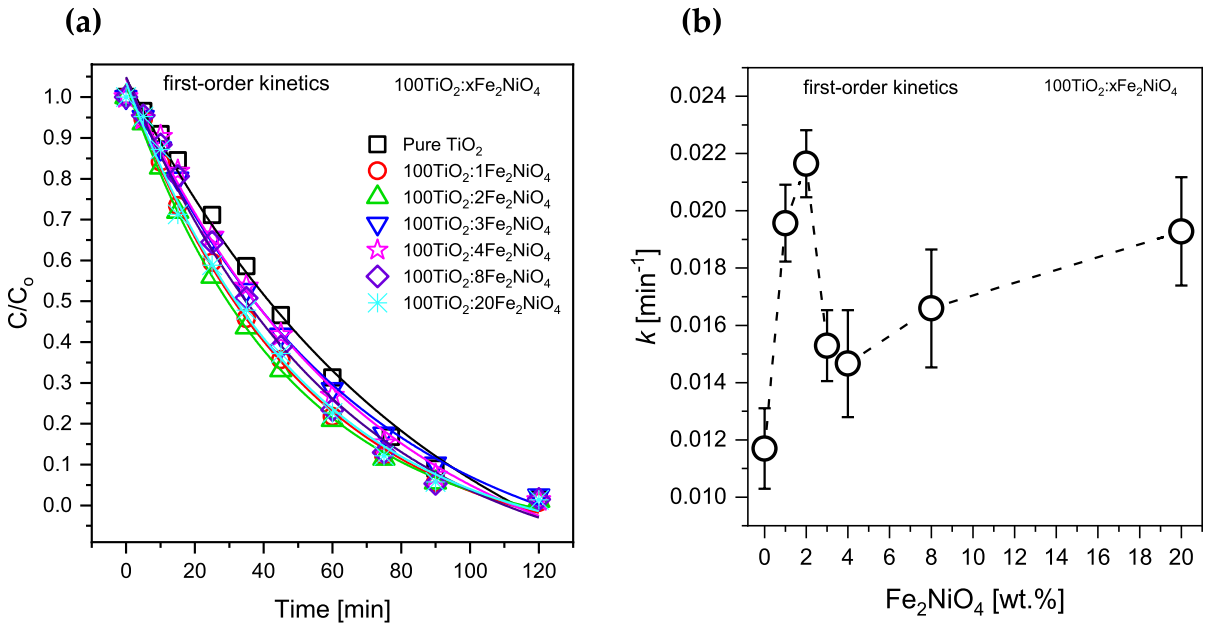

Fig. 8 (**a**) Normalized amplitudes of the aborbance peak at 482 nm from the UV–Vis absorbance spectra in Fig. 6 versus photocatalytic degradation time of AO7 under UV-irradiation of 50 mg/L AO7 initial concentration; catalyst loading is 100 mg/L, solution pH = 3. Solid lines correspond the fitting of the data to a first-order kinetics. (**b**) First-order kinetics reaction constant values deduced from (**a**)

The shape of the absorption spectrum at 2 wt.% Fe_2NiO_4 as a catalyst changed with irradiation time as inferred by the progressing divergence of the bands area and linewidth of the Gaussian function (Fig. 11). The peak position of the all-frequency bands has an obvious red shift (Fig. 11), showing a decrease in solvent polarity. This results in an initial bathochromic shift in the AO7 absorbance maxima, showing that AO7 is either playing a gradual role of an H-bond donor or the dissociated-intermediate products or AO7 are an H-bond donor (Al-Abdallat et al., 2019). According to the preceding discussion and relevant literature, the H-bonded interaction between water and the azo nitrogen atoms in the AO7 has a significant impact on the bands of the major absorption peak. Further irradiation results in a shallow bathochromic shift and an asymptotic approach, reflecting the nature of the AO7 decolonization process and complete mineralization of the dye. Despite differences in absorbance-effected bonding, both bands were shifted in the same pattern, indicating that the H-bond influenced different sites of AO7 molecules. The total absorbance maxima only fit the same function poorly, designating that the time-dependent degradation described by this total absorbance maxima is triggered by multiple processes. Therefore, studying the time-dependent process of photo-oxidization and defining its efficiency based on the attenuation of the convoluted absorbance maxima is misrepresentative and leads to biased results. This is because of the convoluted process being a complicated response to a combination of nonspecific and specific solute–solvent interactions, which are typical for the molecular chemical structure ability to conduct intermolecular interactions, dipole–dipole interactions, the formation–disruption of hydrogen-bonding networks, and hydrophobic/hydrophilic interactions (Ababneh et al., 2018). A similar argument can be made about the amplitudes of the absorbance peaks, since the area under the absorbance peak is more appropriate to describe the convoluted process rather than the peak amplitude. Figure 12 depicts integrated areas deduced individually from the all-frequency bands. The most probable explanation for AO7 degradation is that during the photocatalytic degradation time, H_2O and O_2 molecules diffuse in water and capture the generated holes and electrons, resulting in • OH and superoxide ($\bullet O_2^-$) radicals. The • OH and $\bullet O_2^-$ radicals interact

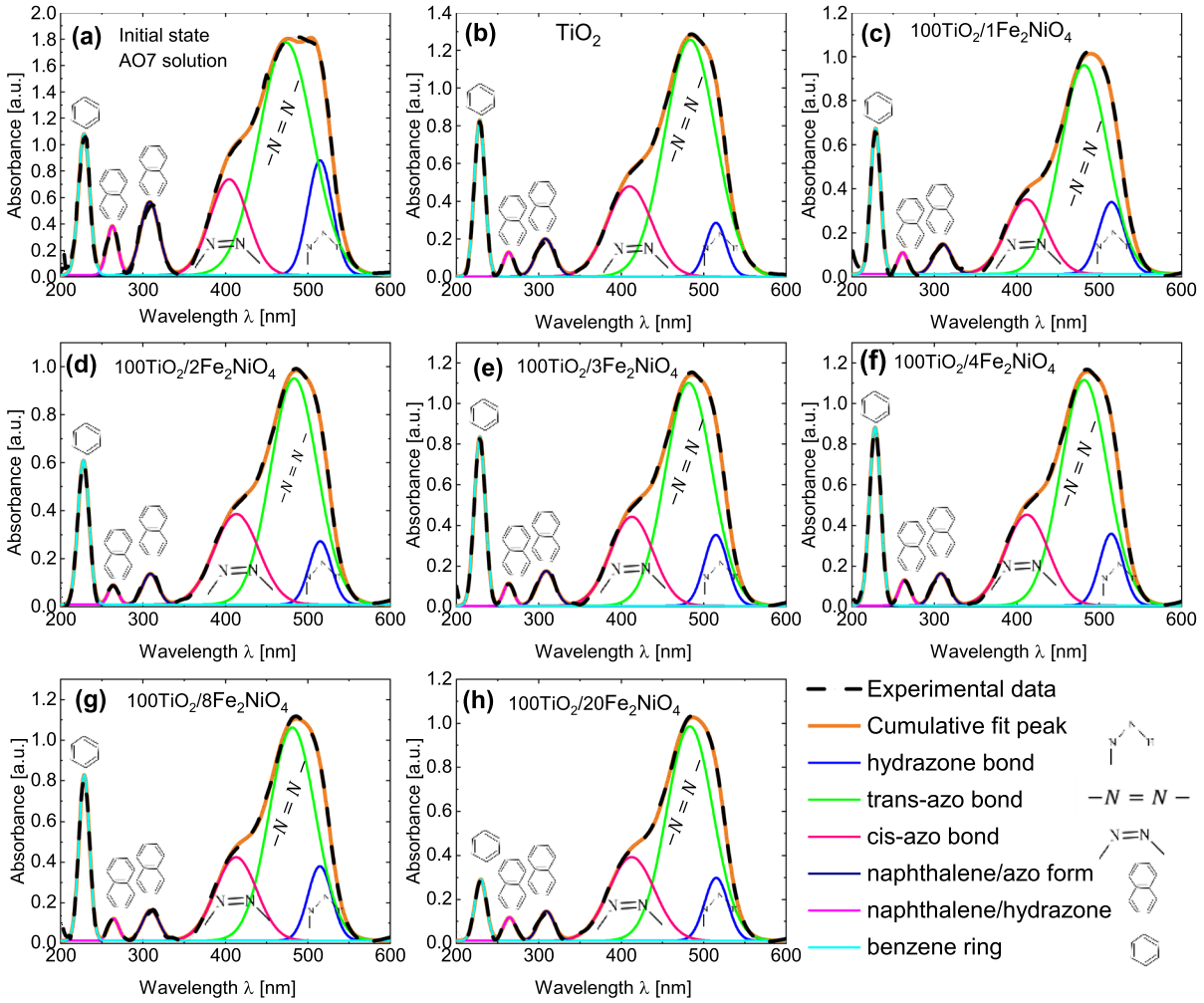

Fig. 9 Peak fits for the absorbance spectra of (**a**) AO7 initial state and AO7 under 25 min of UV–irradiation with (**b**) pure TiO_2 NPs and $100TiO_2$:xFe_2NiO_4 NPs (x = (**c**) 1, (**d**) 2, (**e**) 3, (**f**) 4, (**g**) 8 and (**h**) 20; i.e., 1, 2, 3, 4, 8 and 20 wt.% of Fe_2NiO_4)

destructively with AO7 molecules, resulting in AO7 decolorization. The color of AO7 is determined by the azo bond (−N = N−) and its associated chromophores and auxochromes, where the energy difference between two separate molecular orbitals falls within the visible spectrum (Bureš, 2014). Moreover, the *cis*-state band of the azo form was increased compared to the *trans*-state band of the azo form, where the two bands decreased with increasing UV–irradiation times due to the conversion of trans-isomers to cis-isomers during UV–irradiation (Al-Bataineh et al., 2020b, 2020c).

The impact of pH on the photocatalytic degradation of AO7 in the presence of $100TiO_2$:$2Fe_2NiO_4$ catalyst under UV-irradiation was investigated. Figure 13a illustrates the photocatalytic degradation of $100TiO_2$:$2Fe_2NiO_4$ under UV-irradiation at pH values of 3, 6.5, 9, and 12 at the same conditions of the early measurements (AO7 initial concentration was 50 mg/L, catalyst content was 100 mg/L) were conducted. The data was fitted to the first-order kinetics model and the corresponding first-order kinetic rates were deduced (Fig. 13b). Remarkably, pH of the solution strongly affects the photocatalytic degradation of AO7. Since AO7 is an anionic molecule dye, the pH of the solution affected its adsorption and degradation.

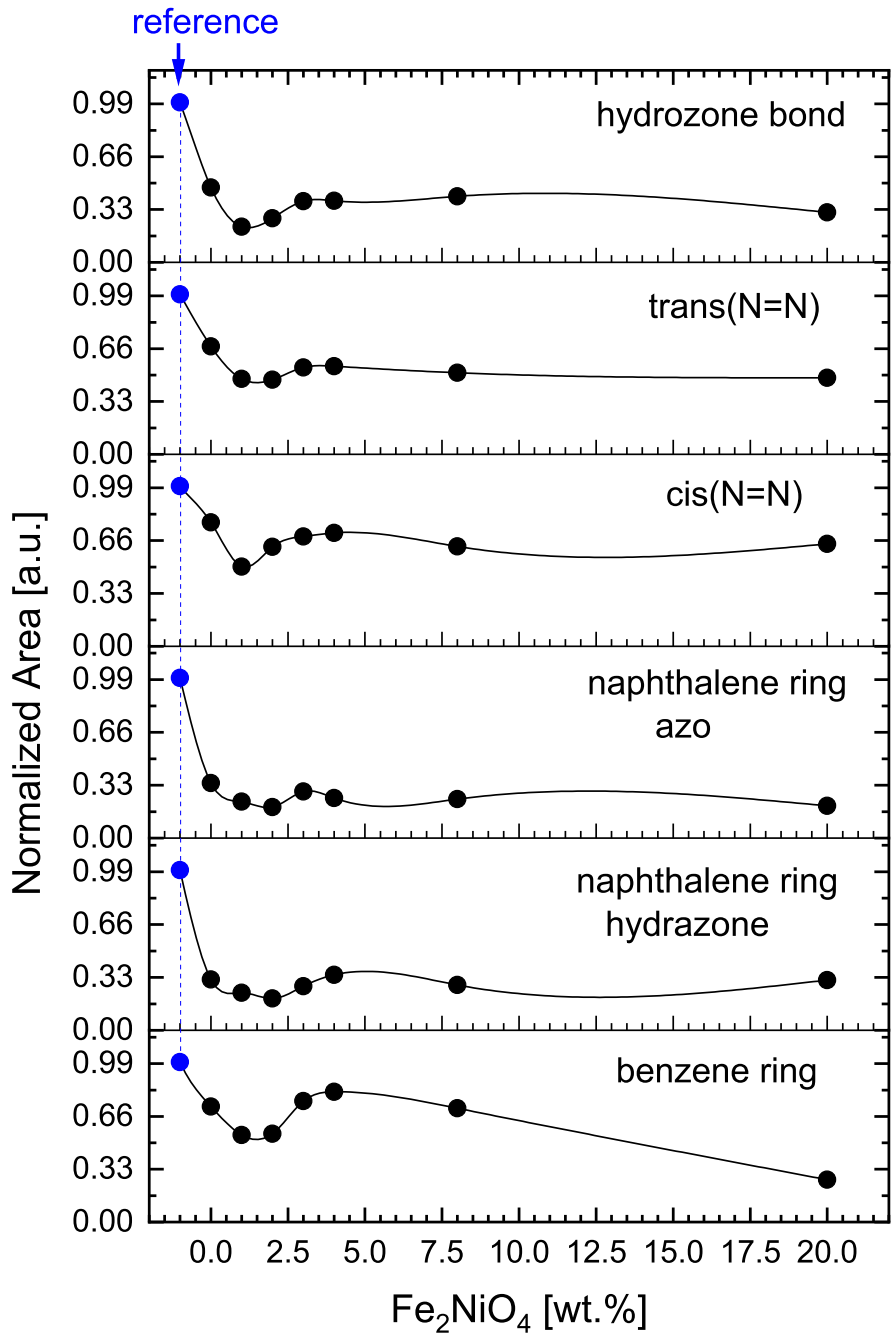

Fig. 10 Integrated area of hydrozone bond, trans(N = N), cis(N = N), naphthalene ring hydrozone and benzene ring under the absorbance peaks of hydrozone bond, trans(N = N), cis(N = N), naphthalene ring hydrozone and benzene ring in AO7 with pure TiO_2 NPs and $100TiO_2$:xFe_2NiO_4 NPs (x = 1, 2, 3, 4, 8 and 20; i.e., 1, 2, 3, 4, 8 and 20 wt.% of Fe_2NiO_4) after 25 min of UV–irradiation

The first-order reaction rate constant at pH = 9 is 16 folds higher than the rate at pH = 6.5, and 7 folds higher than the rates at pH = 3 and pH = 12. At pH 6.5, the net charge on the surface of TiO_2-based photocatalyst is zero. Therefore, adsorption of the negatively charged AO7 dye (anionic pollutant (Khosla et al., 2013)) was minimum since no attraction or repulsion forces were dominant. At pH = 3, the surface of the photocatalyst is a positively charged because of proton abundance, and adsorption of negatively charged AO7 is enhanced. However, due to the high adsorption of AO7, the surface of the catalyst was covered, preventing light photons to penetrate into the catalyst, limiting the degradation rate (Chakrabarti & Dutta,

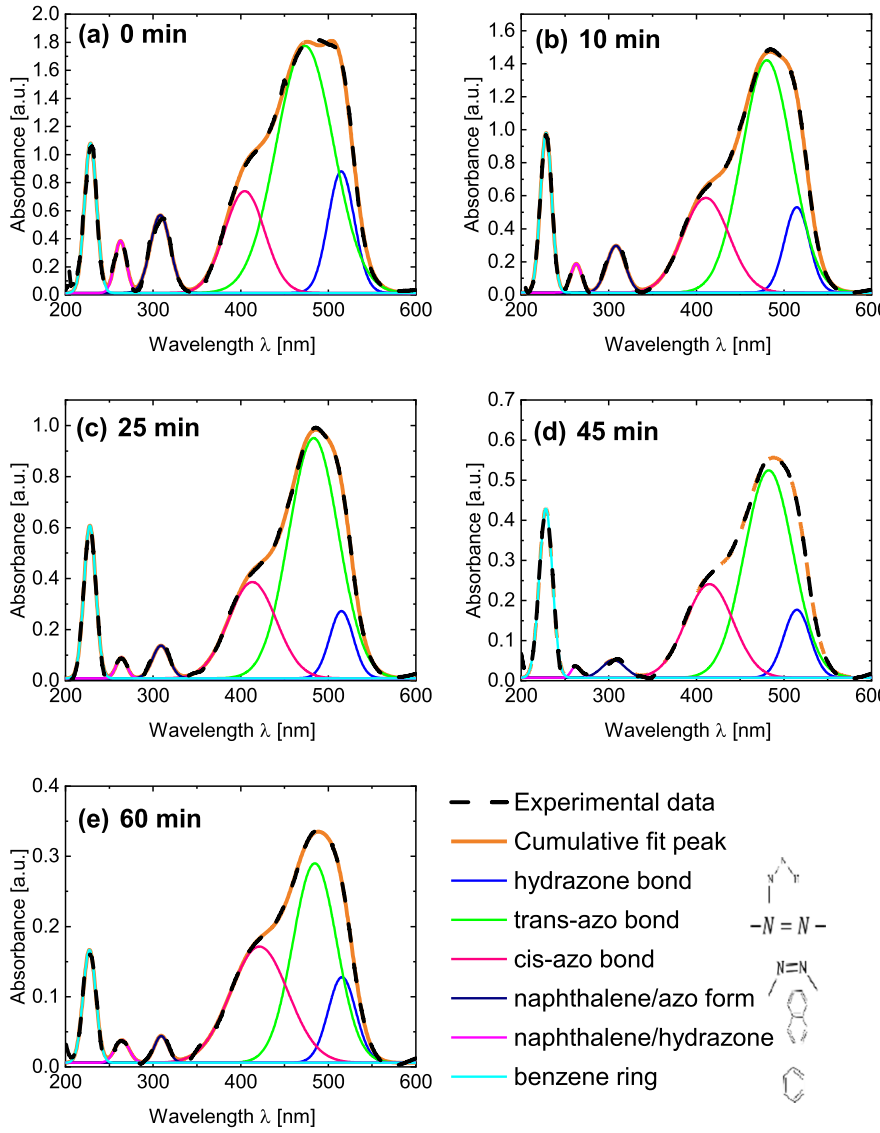

Fig. 11 Peak fits for the absorbance spectra of AO7 for various UV–irradiation times ((a) 0 min, (b) 10 min, (c) 25 min, (d) 45 min and (e) 60 min) using TiO_2:2Fe_2NiO_4 NPs with 2 wt.% of Fe_2NiO_4

2004). Excess OH^- anions (radicals) are present in the solution at higher pH values (=12), resulting in the filling of the active sites of the catalyst and thus preventing reactions from taking place. Because of the OH^- radicals, the catalyst surface becomes negatively charged, leading to a decrease in the adsorption of AO7 ions because of the electrostatic repulsion-inhibiting, resulting in low catalytic degradation.

Finally, the highest degradation performance was observed at pH = 9. A possible explanation is that the AO7 dye exhibits the maximum ionization inside solution at pH = 9, while at pH = 3, the dye may not be ionized at all; therefore, when the pollutant is ionized inside the solution, it is more likely to be degraded more than partially ionized pollutant, resulting in better performance. Besides that, under moderate alkaline conditions (pH = 9), a reasonable amount of OH^- anions are present in the solution, which may aid in generating hydroxyl radicals, resulting in an enhancement in the photodegradation rate.

The degree of ionization of AO7 was estimated using its pKa value (pKa = 11.4 (Pires et al., 2013)) according to the following equation (Watson, 2020):

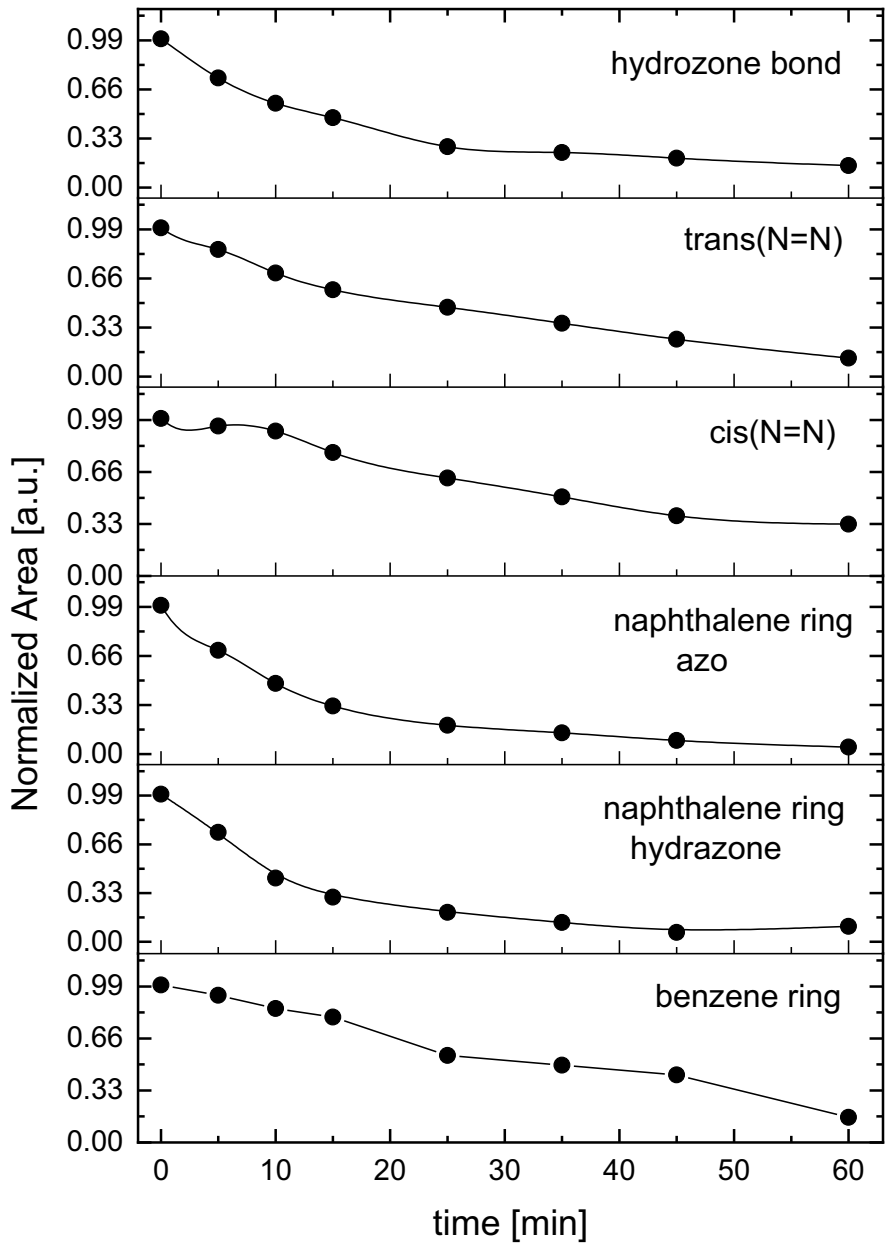

Fig. 12 Integrated area under the absorbance peaks of hydrozone bond, trans(N = N), cis(N = N), naphthalene ring hydrozone and benzene ring in AO7 for various UV–irradiation times using TiO_2:2Fe_2NiO_4 NPs (i.e., 2 wt.% of Fe_2NiO_4)

$$\text{ionization}\% = \frac{10^{pKa-pH}}{1+10^{pKa-pH}} \times 100$$

At pH = 9, over 99.5% ionization can be achieved. It has been reported that there is no strong correlation between the photodegradation performance and the adsorption amount of AO7 on the surface of TiO_2; a decrease in adsorption may not necessarily affect the degradation rate, as the degradation reactions may occur not only inside the catalyst but also inside the bulk solution (Chen et al., 2005).

3.5 COD Removal

COD removal efficiency after 120 min of photocatalysis under UV-irradiation using pure TiO_2 NPs and 100TiO_2:xFe_2NiO_4 NPs (x = 1, 2, 3, 4, 8 and 20; i.e.,

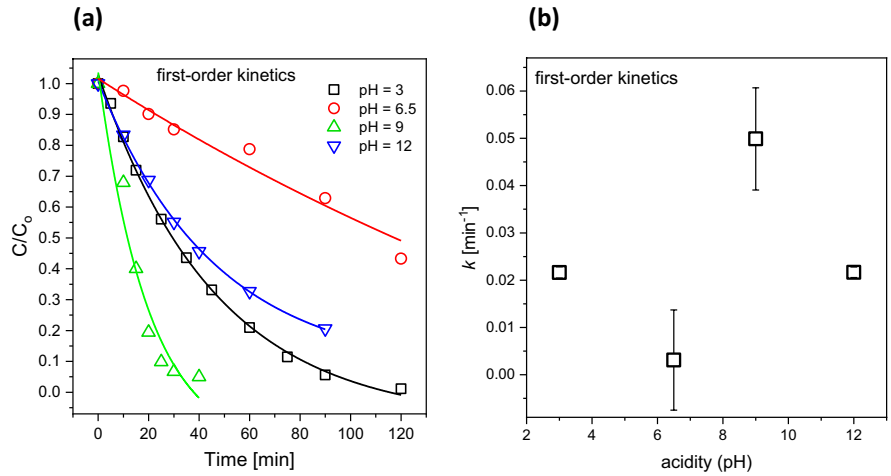

Fig. 13 (**a**) Photocatalytic degradation of $100TiO_2$:$2Fe_2NiO_4$ under UV-irradiation at pH values of 3, 6.5, 9, and 12, where AO7 initial concentration was 50 mg/L, catalyst content was 100 mg/L. The data were fitted to the first-order kinetics model representing with the solid lines. (**b**) The first-order kinetics rate deduced from the fitting in (a) including the fitting error

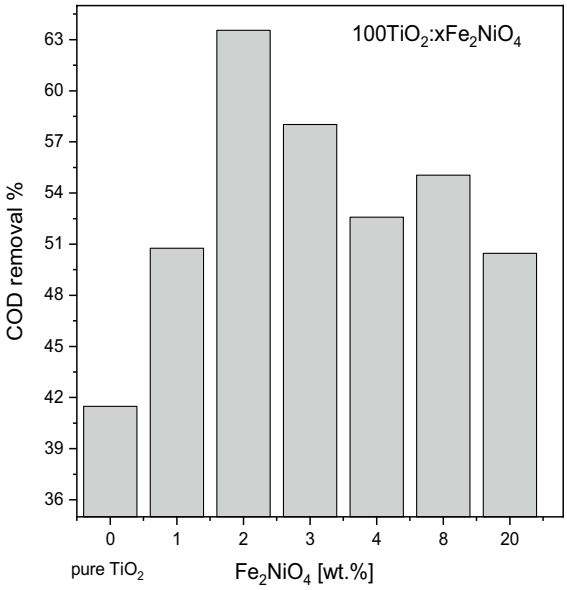

Fig. 14 COD removal efficiency after 120 min of photocatalysis under UV–irradiation with pH = 3. AO7 concentration = 50 mg/L using pure TiO_2 NPs and $100TiO_2$:xFe_2NiO_4 NPs (x = 1, 2, 3, 4, 8 and 20; i.e., 1, 2, 3, 4, 8 and 20 wt.% of Fe_2NiO_4)

1, 2, 3, 4, 8 and 20 wt.% of Fe_2NiO_4) is illustrated in Fig. 14. The highest COD removal efficiency (63.6%) was observed for the $100TiO_2$:$2Fe_2NiO_4$ photocatalyst, compared with the lowest removal efficiency (42%) recorded for pure TiO_2 NPs, confirming the results deduced from the UV–Vis absorbance spectra.

The photocatalytic degradation process of AO7 appears to be highly efficient (95%) in terms of decolorization, but moderately effective in terms of the mineralization (removal of COD) of the contaminants. This may be explained by the formation of reaction intermediates, resulting in chemical fragments that did not decompose over the course of the irradiation experiment (Chiu et al., 2019).

High-resolution ^1H and ^{13}C NMR spectra were measured at a 600.13 MHz (B_0 = 14.1 T) with a Bruker AVANCE III spectrometer with a Bruker ASCEND 600 magnet provided with the multichannel room temperature probehead (Bruker PABBO). High resolution 5 mm borosilicate glass NMR tubes (Boro600-4–8, Deutero GmbH, Kastellaun, Germany) were used for measurements of ^1H at 600.13 MHz and ^{13}C at 240 MHz. Every 500 µL from the samples was mixed with 100 µL of D_2O and 20 µL TSP (1 mM in D_2O) as a reference. The ^1H NMR experiments were acquired using 128 scans (18 min) per measurement, TSP signal was set at zero ppm to calibrate the NMR spectrum. ^{13}C NMR measurement was acquired using ^{13}C channel with 8 k scans (9 h) using the same probehead and same spectrometer. Data acquisition and processing as well as data analysis were conducted with the TopSpin 3.6 software package. Figure 15a and b shows the ^1H NMR spectra of AO7 at NMR frequency of 600.13 MHz at different photocatalytic degradation times (Deg. Time) between 0 and 120 min. The NMR signals of the AO7 and the intermediate groups and moieties appear in the chemical shift range (5–8.7) ppm since most of the functional groups belong to the aromatic rings in AO7 and their intermediate reactants. The ^1H NMR at different degradation times of AO7 shows the typical NMR

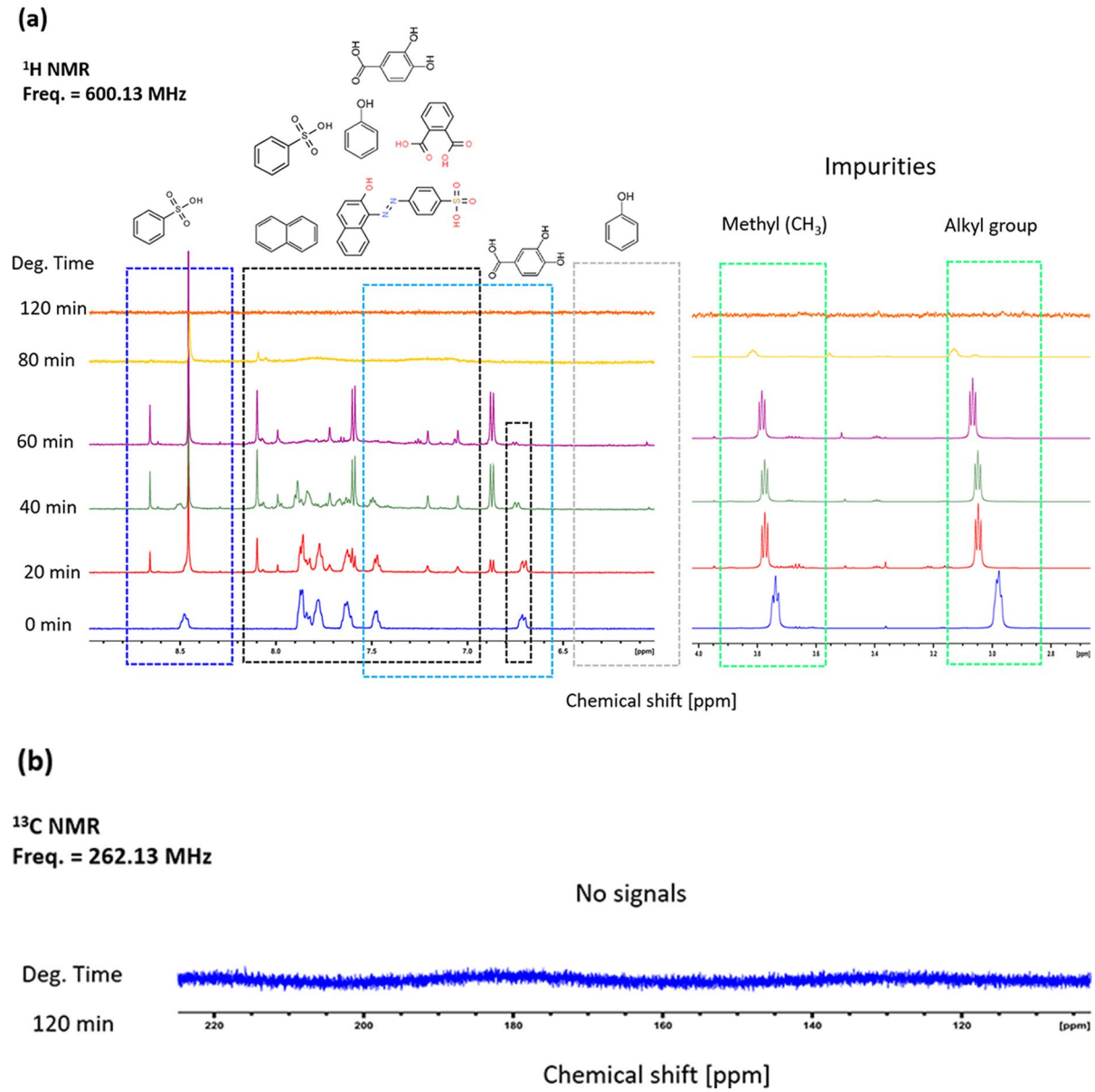

Fig. 15 (**a**) ^{1}H NMR spectra of AO7 at NMR frequency of 600.13 MHz at different photocatalytic degradation time (Deg. Time) between 0 and 120 min. The NMR signals of the AO7 and the intermediate groups and moieties are indicated are indicating by using the dotted squares and their chemical structure attached to the squares, the signals appeared at below 4 ppm are enlarged by factor of 4 × and they are belonging to the methyl and alkyl groups originated from impurities. (**b**) The ^{13}C NMR spectrum of AO7 after 120 min of photocatalytic degradation process, no ^{13}C signals after 8 k scans indicating an organic free solution

spectrum and it broadened because of the high ionic and molecular concentration. The AO7 central frequencies at 7.45 ppm, 7.65 ppm, 7.75 ppm, 7.88 ppm, the signal at 6.7 belongs to the intermediates aromatic that from the start the degradation. The spectrum at time of 20 min showing the resolved signals of AO7 and new signals which belong to naphthalene (7.4 and 7.9) are highly overlapped with the AO7 signals but still can be seen as peak separated. The benzosulfonic acid typically appeared at 7.93 ppm, 6.68 ppm,

7.58 ppm, and 8.65 ppm which obviously existed in the time from 20 min until 60 min and disappeared at 80 and later degradation time. The phenol peaks typically appeared at 6.84, 6.93, and 7.24 indicating that phenol most probably appeared at 60 min and might be attenuated until it is not any more in the spectrum at 100 and 120 min. Several phthalic acid isomers appeared in the aromatic region and characteristically at 7.92 ppm and 8.15 ppm are obviously showing up until at 80 min of degradation. The NMR spectrum after 40 min of degradation shows similar peaks that are in the spectrum at 20 min with less signal broadening and magnitude indicating less concentration and less ionic. The signals appearing at below 4 ppm are enlarged by a factor of 4 × and they belong to the methyl and alkyl groups that originated from impurities. Remarkably, there are no signals can be observed in the ^{1}H NMR spectrum at 120 min indicating complete degradation of the AO7 and all its intermediates. The signal of methyl and alkyl groups from the impurities also depredated in total. To validate the results and to prove that no organic groups that might be bonded to other than protons, ^{13}C NMR measurements were conducted at 120 min, since if we have any other organics, it will definitely appear in the ^{13}C spectrum. Figure 15b shows the ^{13}C NMR spectrum of AO7 after 120 min of photocatalytic degradation process; the spectrum does not exhibit any ^{13}C signals indicating the sample (solution) is free of any possible organic groups which have no proton that can be seen with ^{1}H NMR.

Based on the above results, AO7 degradation is a combined process since AO7 moieties degrade in a somewhat sequential and parallel manner. The C–N single bond between the azo bond and the benzene ring is the first degradation bond, and this is can be supported by the disappearance of the C–N vibrational band of the aromatic amine in the FTIR spectra, as reported in the literature (Lau et al., 2014; Zhu et al., 2012). The breakdown of the C–N bond leads to the formation of benzenesulfonic acid ($C_6H_6SO_3$) and hydroxy-naphthalene-diazonium ($C_{10}H_8N_2O$). Meanwhile, the benzenesulfonic acid ionization constant of releasing sodium ion (Na^+) to the solution changed to different values leading to a change in the solution acidity. The primary reaction was further degraded to form lower-molecular weight products, and the hydroxy-naphthalene-diazonium was then transformed into naphthalene-diazonium ($C_{10}H_8N_2$) according to Ghodake et al. (2011). Due to the extended valence shells of the large sulfur atom, the desulfonation reaction of benzenesulfonic acid into an aryl sulfonic group and the benzene ring occurs in parallel (Ababneh et al., 2018). The benzene ring then reacts with the OH^- to produce phenol, and the naphthalene-diazonium transforms into

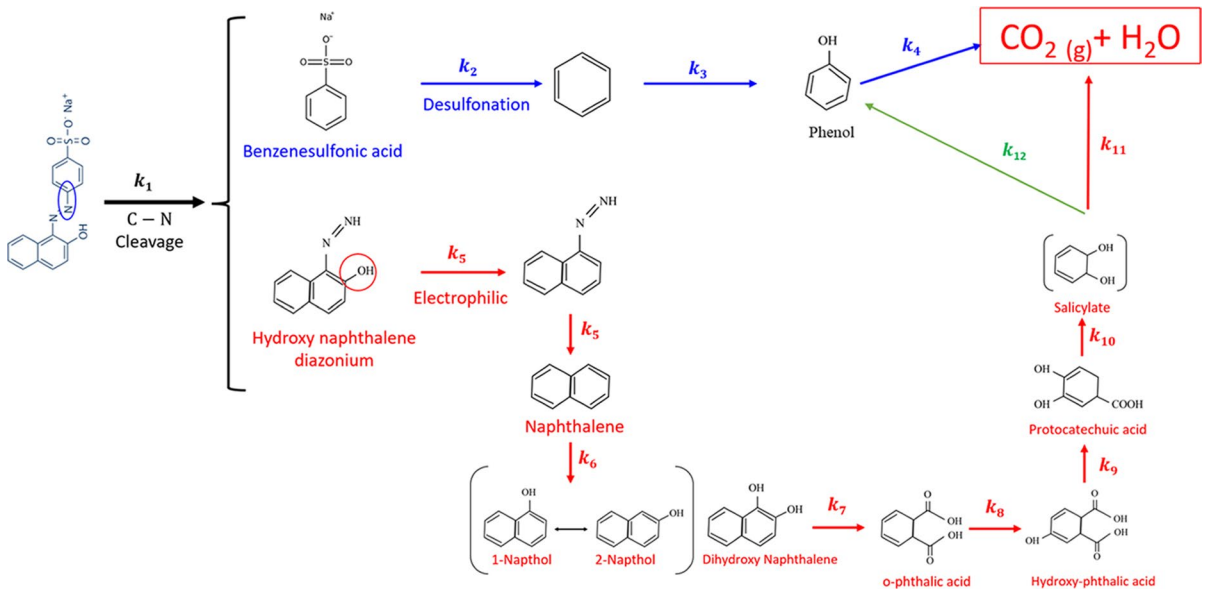

Fig. 16 Photodegradation pathway of AO7 based on the results from this work and literature review

benzene-1,2-dicarboxylic acid. Finally, the phenol and benzene-1,2-dicarboxylic acid degrade to carbon dioxide (CO_2) and water, respectively (Mani et al., 2019). Figure 16 depicts a diagram of the aforementioned degradation pathways.

The above degradation pathways and associated rates (k_1 through k_{12}) may explain the loose fitting of the experimental data to the first-order kinetics model of AO7 degradation, and thus this single kinetic rate is somewhat the average of the overall process. The average fit is still acceptable and can express the process and can be referred to as the apparent kinetic rate.

3.6 Electrical Energy Consumption

The electrical power consumption of the photocatalysis of 1.8 L of 50 mg/L AO7 aqueous solutions under UV light using 100 mg/L $100TiO_2$:$2Fe_2NiO_4$ catalysts along with a comparison with similar systems reported in the literature are presented in Table 3. In terms of energy consumption, the proposed optimum system in this research demonstrated exceptional electrical energy utilization. For the same removal efficiencies (~90%), 50.3 kWh/m^3 electric energy consumption was calculated for degradation of high concentrations of AO7 (50 mg/L), compared to the lowest consumption (43 kWh/m^3) of lower concentrations of AO7 (10 mg/L). This is due to the highly efficient design of the reactor, in which the UV lamp was immersed inside the reactor to achieve maximum energy utilization and efficiency.

Moreover, according to Table 3, the electrical energy consumption for the present system was almost the lowest among all the presented recent researches, despite the fact that the concentration was around 60% higher (requires more energy), demonstrating that the model system used in this study is significantly more efficient.

4 Conclusions

The calculated size distribution from SEM micrographs for TiO_2 NPs, $100TiO_2$:$2Fe_2NiO_4$, and $100TiO_2$:$3Fe_2NiO_4$ nanocomposites NPs is in the range of 15–25 nm while for pure Fe_2NiO_4, is in the range of 30–50 nm, being all of spherical shape. The size distribution in an aqueous solution was also measured using DLS and was found to agglomerate in clusters with sizes up to 250 nm. The UV-light-induced photocatalysis was found to follow first-order kinetics, and the highest degradation performance was observed at pH = 9, which corresponds to the maximum degree of AO7 dye ionization inside the solution. The most efficient coupling rate was achieved by using 2 wt.% of Fe_2NiO_4 NPs of with a relative improvement in the kinetic rate constant of 87% compared to that of pure TiO_2 NPs: This is ascribed to the enhancement of electron–hole pairs separation and size of the unit cell volume that was the largest at 2 wt.%. Spectral deconvolution analysis was performed to quantify the several frequency absorbance bands of the AO7 over the course of 25 min of UV–irradiation, and the results revealed non-monotonic spectral dynamics including peak wavelength shifts, absolute amplitude, and area changes for the AO7 bands.

Table 3 Comparison of E_{EO} (kWh/m^3) with some recent studies in the literature for photocatalysis of different organic pollutants using TiO_2-based photocatalyst

Pollutant	Conc [mg/L]	Light source	Input power [W]	Irradiation time [min]	Removal [%]	E_{EO} [kWh/m^3]	Ref
AO7	50	Mercury lamp	500	25	90	50	Present research
AO7	10	Visible-LEDs	10	60	90	43	Mancuso et al., 2020) (2020)
Crystal violet dye	10	UV-lamps	140	40	90	63	Vaiano et al., 2019) (2019)
Methylene Blue	10	Xenon lamp	450	240	60	160	Zhou & Wang, 2014) (2014)
Phenol	20	Metal halide lamp	575	48	90	250	Sun et al., 2013) (2013)
Ciprofloxacin	20	LEDs lamp	36	360	636	120	Suwannaruang et al., 2020) (2020)

Acknowledgements This work was supported by the Deanship of Research, Jordan University of Science and Technology, Irbid, Jordan under Grant No. 2020/407. The scientific support by the Ministerium für Innovation, Wissenschaft und Forschung des Landes Nordrhein-Westfalen, the Senatsverwaltung für Wirtschaft, Technologie und Forschung des Landes Berlin, and the Bundesministerium für Bildung und Forschung is gratefully acknowledged. Our thanks also to Prof. Ahmad A. Ahmad for helping our members to use thin films laboratory.

Data Availability The data are available on request.

Declarations

Conflict of Interest The authors declare no competing interests.

References

Ababneh, R., Telfah, A., Jum'h, I., Abudayah, M., Al-Abdallat, Y., Lambert, J., & Hergenröder, R. (2018). 1h nmr spectroscopy to investigate the kinetics and the mechanism of proton charge carriers ionization and transportation in hydrophilic/hydrophobic media: Methyl sulfonic acid as a protonic ion source in water/alcohol binary mixtures. *Journal of Molecular Liquids, 265*, 621–628.

Ahmad, A. A., Al-Bataineh, Q. M., Alsaad, A. M., Al-Nawafleh, D. M., Al-Nawafleh, A. M., & Telfah, A. D. (2021a). Synthesis and characterization of thin films based on azobenzene derivative anchored to CeO_2 nanoparticle for photoswitching applications. *Photochemistry and Photobiology, 98*(4), 823–830.

Ahmad, A. A., Al-Bataineh, Q. M., Al-Nawafleh, D. M., & Telfah, A. D. (2021b). Photoisomerization kinetics of photoswitchable thin films based on nanostructure/molecular layers of AlN-AO7. *Photochemistry and Photobiology, 98*(4), 831–842.

Akl, A. A., & Hassanien, A. (2015). Microstructure and crystal imperfections of nanosized CdSxSe1− x thermally evaporated thin films. *Superlattices and Microstructures, 85*, 67–81.

Al-Abdallat, Y., Jum'h, I., Al Bsoul, A., Jumah, R., & Telfah, A. (2019). Photocatalytic degradation dynamics of methyl orange using coprecipitation synthesized fe 3 o 4 nanoparticles. *Water, Air, & Soil Pollution, 230*(12), 1–16.

Al-Bataineh, Q. M., Alsaad, A., Ahmad, A., & Al-Sawalmih, A. (2019). Structural, electronic and optical characterization of ZnO thin film-seeded platforms for ZnO nanostructures: Sol–gel method versus ab initio calculations. *Journal of Electronic Materials, 48*(8), 5028–5038.

Al-Bataineh, Q. M., Telfah, M., Ahmad, A. A., Alsaad, A. M., Qattan, I. A., Baaziz, H., Charifi, Z., & Telfah, A. (2020). Synthesis, crystallography, microstructure, crystal defects, optical and optoelectronic properties of ZnO: CeO_2 mixed oxide thin films. *Photonics, 7*(4), 112.

Al-Bataineh, Q. M., Ahmad, A., Alsaad, A., Qattan, I., Bani-Salameh, A. A., & Telfah, A. D. (2020). Kinematics of photoisomerization processes of PMMA-BDK-MR polymer composite thin films. *Polymers, 12*(6), 1275.

Al-Bataineh, Q. M., Ahmad, A. A., Alsaad, A. M., & Telfah, A. (2020). New insight on photoisomerization kinetics of photo-switchable thin films based on azobenzene/graphene hybrid additives in polyethylene oxide. *Polymers, 12*(12), 2954.

Al-Mamun, M., Kader, S., Islam, M., & Khan, M. (2019). Photocatalytic activity improvement and application of UV-TiO_2 photocatalysis in textile wastewater treatment: A review. *Journal of Environmental Chemical Engineering, 7*(5), 103248.

Alsaad, A., Ahmad, A., Qattan, I., Al-Bataineh, Q. M., & Albataineh, Z. (2020). Structural, optoelectrical, linear, and nonlinear optical characterizations of dip-synthesized undoped ZnO and group III elements (B, Al, Ga, and In)-doped ZnO thin films. *Crystals, 10*(4), 252.

Al-Tohamy, R., Ali, S. S., Li, F., Okasha, K. M., Mahmoud, Y.A.-G., Elsamahy, T., Jiao, H., Fu, Y., & Sun, J. (2022). A critical review on the treatment of dye-containing wastewater: Ecotoxicological and health concerns of textile dyes and possible remediation approaches for environmental safety. *Ecotoxicology and Environmental Safety, 231*, 113160.

Bauer, C., Jacques, P., & Kalt, A. (1999). Investigation of the interaction between a sulfonated azo dye (AO7) and a TiO_2 surface. *Chemical Physics Letters, 307*(5–6), 397–406.

Bolton, J. R., Bircher, K. G., Tumas, W., & Tolman, C. A. (2001). Figures-of-merit for the technical development and application of advanced oxidation technologies for both electric-and solar-driven systems (IUPAC Technical Report). *Pure and Applied Chemistry, 73*(4), 627–637.

Bureš, F. (2014). Fundamental aspects of property tuning in push–pull molecules. *RSC Advances, 4*(102), 58826–58851.

Chakrabarti, S., & Dutta, B. K. (2004). Photocatalytic degradation of model textile dyes in wastewater using ZnO as semiconductor catalyst. *Journal of Hazardous Materials, 112*(3), 269–278.

Chen, Y., Yang, S., Wang, K., & Lou, L. (2005). Role of primary active species and TiO_2 surface characteristic in UV-illuminated photodegradation of Acid Orange 7. *Journal of Photochemistry and Photobiology a: Chemistry, 172*(1), 47–54.

Chiu, Y.-H., Chang, T.-F.M., Chen, C.-Y., Sone, M., & Hsu, Y.-J. (2019). Mechanistic insights into photodegradation of organic dyes using heterostructure photocatalysts. *Catalysts, 9*(5), 430.

Chung, K.-T. (2016). Azo dyes and human health: A review. *Journal of Environmental Science and Health, Part C, 34*(4), 233–261.

Feng, W., Nansheng, D., & Helin, H. (2000). Degradation mechanism of azo dye CI reactive red 2 by iron powder reduction and photooxidation in aqueous solutions. *Chemosphere, 41*(8), 1233–1238.

Ghodake, G., Jadhav, U., Tamboli, D., Kagalkar, A., & Govindwar, S. (2011). Decolorization of textile dyes and degradation of mono-azo dye amaranth by Acinetobacter calcoaceticus NCIM 2890. *Indian Journal of Microbiology, 51*(4), 501–508.

Habibi, M. H., & Fakhri, F. (2017). Hydrothermal synthesis of nickel iron oxide nano-composite and application as magnetically separable photocatalyst for degradation of Solar Blue G dye. *Journal of Materials Science: Materials in Electronics, 28*(19), 14091–14096.

Haider, A. J., Jameel, Z. N., & Al-Hussaini, I. H. (2019). Review on: Titanium dioxide applications. *Energy Procedia, 157*, 17–29.

Han, F., Kambala, V., Dharmarajan, R., Liu, Y., & Naidu, R. (2018). Photocatalytic degradation of azo dye acid orange 7 using different light sources over Fe3+-doped TiO_2 nanocatalysts. *Environmental Technology & Innovation, 12*, 27–42.

Horiuchi, S., Tokunaga, Y., Giovannetti, G., Picozzi, S., Itoh, H., Shimano, R., Kumai, R., & Tokura, Y. (2010). Above-room-temperature ferroelectricity in a single-component molecular crystal. *Nature, 463*(7282), 789.

Hossen, A., Chowdhury, T., & Mondal, I. (2022). Purification of textile dye-contained wastewater by three alternative promising techniques: Adsorption, Biodegradation and Advanced Oxidation Processes (AOPs)-A review. *J Textile Eng Fashion Technol, 8*(3), 96–98.

Iervolino, G., Zammit, I., Vaiano, V., & Rizzo, L. (2020). Limitations and prospects for wastewater treatment by UV and visible-light-active heterogeneous photocatalysis: A critical review. *Topics in Current Chemistry, 378*, 7.

Ijadpanah-Saravy, H., Safari, M., Khodadadi-Darban, A., & Rezaei, A. (2014). Synthesis of titanium dioxide nanoparticles for photocatalytic degradation of cyanide in wastewater. *Analytical Letters, 47*(10), 1772–1782.

Khasawneh, O. F. S., & Palaniandy, P. (2021). Removal of organic pollutants from water by Fe_2O_3/TiO_2 based photocatalytic degradation: A review. *Environmental Technology & Innovation, 21*, 101230.

Khosla, E., Kaur, S. & Dave, P. N. (2013). Mechanistic study of adsorption of acid orange-7 over aluminum oxide nanoparticles. *Journal of Engineering, 2013*, 593534.

Lau, Y.-Y., Wong, Y.-S., Teng, T.-T., Morad, N., Rafatullah, M., & Ong, S.-A. (2014). Coagulation-flocculation of azo dye Acid Orange 7 with green refined laterite soil. *Chemical Engineering Journal, 246*, 383–390.

Maeda, H., Maeda, T., & Mizuno, K. (2012). Absorption and fluorescence spectroscopic properties of 1-and 1, 4-silyl-substituted naphthalene derivatives. *Molecules, 17*(5), 5108–5125.

Mancuso, A., Sacco, O., Sannino, D., Pragliola, S., & Vaiano, V. (2020). Enhanced visible-light-driven photodegradation of Acid Orange 7 azo dye in aqueous solution using Fe-N co-doped TiO_2. *Arabian Journal of Chemistry, 13*(11), 8347–8360.

Mani, P., Fidal, V., Bowman, K., Breheny, M., Chandra, T., Keshavarz, T., & Kyazze, G. (2019). Degradation of azo dye (acid orange 7) in a microbial fuel cell: Comparison between anodic microbial-mediated reduction and cathodic laccase-mediated oxidation. *Frontiers in Energy Research, 7*, 101.

Manzoor, J., & Sharma, M. (2020). Impact of textile dyes on human health and environment. *Impact of textile dyes on public health and the environment* (pp. 162–169). IGI Global.

McManamon, C., O'Connell, J., Delaney, P., Rasappa, S., Holmes, J. D., & Morris, M. A. (2015). A facile route to synthesis of S-doped TiO_2 nanoparticles for photocatalytic activity. *Journal of Molecular Catalysis a: Chemical, 406*, 51–57.

Nasr, M., Eid, C., Habchi, R., Miele, P., & Bechelany, M. (2018). Recent progress on titanium dioxide nanomaterials for photocatalytic applications. *Chemsuschem, 11*(18), 3023–3047.

Nguyen, C. H., Fu, C.-C., & Juang, R.-S. (2018). Degradation of methylene blue and methyl orange by palladium-doped TiO_2 photocatalysis for water reuse: Efficiency and degradation pathways. *Journal of Cleaner Production, 202*, 413–427.

Perera, H. (2019). Removal of acid orange 7 dye from wastewater: Review. *Int J Waste Resour, 9*(367), 2.

Pires, M. J. R., Ferra, M. I. A., & Marques, A. M. (2013). Ionization of Acid Orange 7 in various ionic media. *Journal of Chemical & Engineering Data, 58*(8), 2181–2186.

Rashid, R., Shafiq, I., Akhter, P., Iqbal, M. J., & Hussain, M. (2021). A state-of-the-art review on wastewater treatment techniques: The effectiveness of adsorption method. *Environmental Science and Pollution Research, 28*(8), 9050–9066.

Rehman, S., Ullah, R., Butt, A., & Gohar, N. (2009). Strategies of making TiO_2 and ZnO visible light active. *Journal of Hazardous Materials, 170*(2–3), 560–569.

Robotti, M., Dosta, S., Cano, I., Concustell, A., Cinca, N., & Guilemany, J. (2016). Attrition and cryogenic milling powder production for low pressure cold gas spray and composite coatings characterization. *Advanced Powder Technology, 27*(4), 1257–1264.

Samsami, S., Mohamadizaniani, M., Sarrafzadeh, M.-H., Rene, E. R., & Firoozbahr, M. (2020). Recent advances in the treatment of dye-containing wastewater from textile industries: Overview and perspectives. *Process Safety and Environmental Protection, 143*, 138–163.

Santhosh, C., Velmurugan, V., Jacob, G., Jeong, S. K., Grace, A. N., & Bhatnagar, A. (2016). Role of nanomaterials in water treatment applications: A review. *Chemical Engineering Journal, 306*, 1116–1137.

Silva, A. C., Silvestre, A. J., Freire, C. S., & Vilela, C. (2021). *"Modification of textiles for functional applications," Fundamentals of Natural Fibres and Textiles* (pp. 303–365). Elsevier.

Sun, H., Zhou, G., Liu, S., Ang, H. M., Tadé, M. O., & Wang, S. (2013). Visible light responsive titania photocatalysts codoped by nitrogen and metal (Fe, Ni, Ag, or Pt) for remediation of aqueous pollutants. *Chemical Engineering Journal, 231*, 18–25.

Suwannaruang, T., Hildebrand, J. P., Taffa, D. H., Wark, M., Kamonsuangkasem, K., Chirawatkul, P., & Wantala, K. (2020). Visible light-induced degradation of antibiotic ciprofloxacin over Fe–N–TiO_2 mesoporous photocatalyst with anatase/rutile/brookite nanocrystal mixture. *Journal of Photochemistry and Photobiology A: Chemistry, 391*, 112371.

Suzuki, M., Suzuki, Y., Uzuka, K., & Kawase, Y. (2020). Biological treatment of non-biodegradable azo-dye enhanced by zero-valent iron (ZVI) pre-treatment. *Chemosphere, 259*, 127470.

Thekkedath, A., Sugaraj, S., & Sridharan, K. (2022). *"Nanomaterials in advanced oxidation processes (AOPs) in anionic dye removal," Advanced Oxidation Processes in Dye-Containing Wastewater* (pp. 129–165). Springer.

Vaiano, V., Sacco, O., & Sannino, D. (2019). Electric energy saving in photocatalytic removal of crystal violet dye through the simultaneous use of long-persistent blue phosphors, nitrogen-doped TiO_2 and UV-light emitting diodes. *Journal of Cleaner Production, 210*, 1015–1021.

Watson, D. G. (2020). *Pharmaceutical analysis E-book: a textbook for pharmacy students and pharmaceutical chemists*. Elsevier Health Sciences.

Williamson, G., & Smallman, R. (1956). III. Dislocation densities in some annealed and cold-worked metals from measurements on the X-ray debye-scherrer spectrum. *Philosophical Magazine, 1*(1), 34–46.

Zaheer, Z., Bawazir, W. A., Al-Bukhari, S. M., & Basaleh, A. S. (2019). Adsorption, equilibrium isotherm, and thermodynamic studies to the removal of acid orange 7. *Materials Chemistry and Physics, 232*, 109–120.

Zhou Z. & Wang, H. (2014). Noncompensated codoping TiO_2 nanowires: The enhanced visible light photocatalytic properties. *International Journal of Photoenergy, 2014*. https://doi.org/10.1155/2014/568185

Zhu, N., Gu, L., Yuan, H., Lou, Z., Wang, L., & Zhang, X. (2012). Degradation pathway of the naphthalene azo dye intermediate 1-diazo-2-naphthol-4-sulfonic acid using Fenton's reagent. *Water Research, 46*(12), 3859–3867.